Article

Cell Systems

Systematic Quantification of Population Cell Death Kinetics in Mammalian Cells

Graphical Abstract

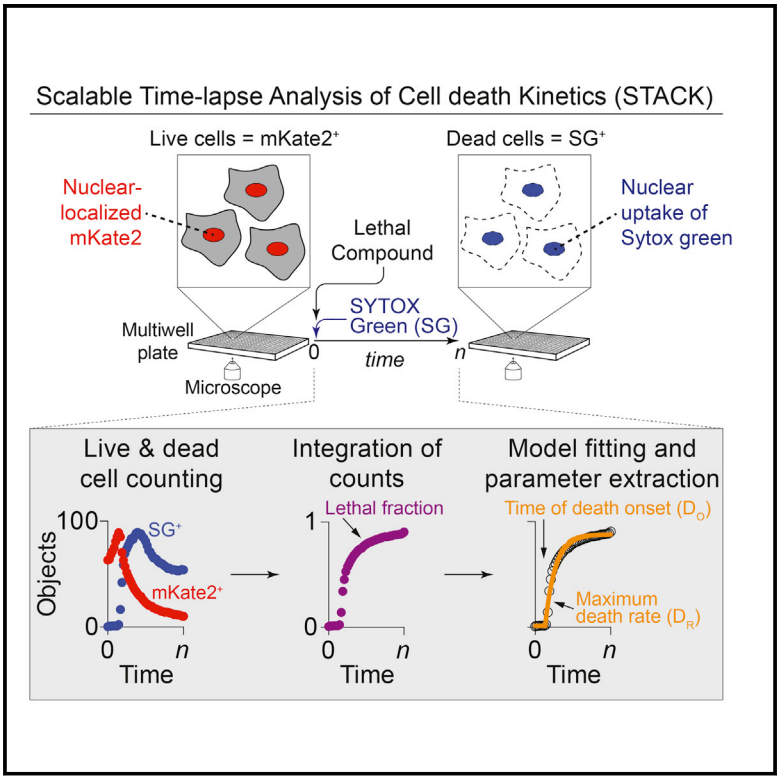

Authors

Giovanni C. Forcina, Megan Conlon, Alex Wells, Jennifer Yinuo Cao, Scott J. Dixon

Correspondence

sjdixon@stanford.edu

In Brief

We describe scalable time-lapse analysis of cell death (STACK) as a new method to investigate population-level cell death kinetics in mammalian cells. We observe considerable diversity in lethal compound-induced cell death kinetics between compounds, compound concentrations, and cell lines.

Highlights

- STACK is a method to quantify population-level cell death kinetics
- Cell death kinetics vary between lethal compound classes and cell lines
- Cell death kinetics provide a means to classify lethal compound activity
- 13 compounds induce a rapid-onset lethal phenotype

Forcina et al., 2017, Cell Systems *4*, 600–610
June 28, 2017
http://dx.doi.org/10.1016/j.cels.2017.05.002

OPEN ACCESS
CellPress

Cell Systems
Article

Systematic Quantification of Population Cell Death Kinetics in Mammalian Cells

Giovanni C. Forcina,[1] Megan Conlon,[1] Alex Wells,[1] Jennifer Yinuo Cao,[1] and Scott J. Dixon[1,2,*]
[1]Department of Biology, Stanford University, Room 104, 337 Campus Drive, Stanford, CA 94305, USA
[2]Lead Contact
*Correspondence: sjdixon@stanford.edu
http://dx.doi.org/10.1016/j.cels.2017.05.002

SUMMARY

Cytotoxic compounds are important drugs and research tools. Here, we introduce a method, scalable time-lapse analysis of cell death kinetics (STACK), to quantify the kinetics of compound-induced cell death in mammalian cells at the population level. STACK uses live and dead cell markers, high-throughput time-lapse imaging, and mathematical modeling to determine the kinetics of population cell death over time. We used STACK to profile the effects of over 1,800 bioactive compounds on cell death in two human cancer cell lines, resulting in a large and freely available dataset. 79 potent lethal compounds common to both cell lines caused cell death with widely divergent kinetics. 13 compounds triggered cell death within hours, including the metallophore zinc pyrithione. Mechanistic studies demonstrated that this rapid onset lethal phenotype was caused in human cancer cells by metabolic disruption and ATP depletion. These results provide the first comprehensive survey of cell death kinetics and analysis of rapid-onset lethal compounds.

INTRODUCTION

Cell death is a fundamental biological process that can be triggered by diverse lethal stimuli. Detergents and other harsh treatments that directly permeabilize the plasma membrane can kill the cell rapidly and without activating a specific regulated cell death pathway (Wolpaw et al., 2011). By contrast, cell death in response to physiological signals, stresses, or lethal compounds that engage specific protein targets can take many hours or even days (Biton and Ashkenazi, 2011; Dixon et al., 2012; Lu et al., 2014; Shimizu et al., 2004). Cell death under these conditions is initiated by specific signaling cascades or metabolic disruptions and is executed through a highly ordered, stepwise process. For example, during apoptosis, a key step in cell death execution involves permeabilization of the mitochondrial outer membrane by the pore-forming proteins BCL2-associated X protein (BAX) and BCL2-antagonist/killer (BAK) (Wei et al., 2001), while during ferroptotic cell death the iron-dependent, oxidative destruction of membrane lipids likely causes terminal membrane permeabilization (Dixon et al., 2012).

The time between exposure to a given lethal stimulus and terminal membrane permeabilization is an important period. In addition to enabling the ordered execution of cell death, this time can allow for the release of "danger signals" to neighboring cells and, sometimes, for the cell to return from the brink of death if the lethal stimulus is ultimately removed (Gong et al., 2017; Tang et al., 2012). For reasons that remain poorly understood, cell death kinetics vary considerably between lethal stimuli, cell lines, and cell death pathways, as well as between individual cells within the same population (Bernheim et al., 1977; Biton and Ashkenazi, 2011; Dixon et al., 2012; Lu et al., 2014; Shimizu et al., 2004; Spencer et al., 2009; Vanden Berghe et al., 2010). A major goal of the present work was to develop a means to quantify this variability in cell death kinetics at the population level, as this knowledge may enhance our understanding of different lethal pathways, improve the classification of lethal perturbations, and help identify new drugs that act through unique mechanisms (Grootjans et al., 2016; Hafner et al., 2016; Harris et al., 2016; Palchaudhuri et al., 2015; Tyson et al., 2012).

Profiling the response of cancer cells to different lethal compounds can provide insight into the regulation of specific cell death pathways and may lead to the discovery of new targeted therapies (Dixon et al., 2012; Haverty et al., 2016; Wolpaw et al., 2011). These large-scale studies typically investigate cell death at a single, arbitrary time point (e.g., 48 or 72 hr) that provides no insight into the kinetics of cell death or whether these kinetics differ between treatments. Moreover, in these and many other studies, cell death is not examined directly, but rather using bulk biochemical measures of overall population metabolic activity or DNA content. These methods are fast and inexpensive, but subject to technical confounds that can interfere with the analysis of cell death (Chan et al., 2013). Methods that directly assess cell death within a population could help address these limitations.

To directly measure population cell death and assess the kinetics of this process we developed a method called STACK. This method uses live and dead cell markers, high-throughput time-lapse imaging, and mathematical modeling to capture the kinetics of cell death in terms of the length of time between the addition of a lethal stimulus and the onset of cell death, and the maximum rate of this process within the population. We find differences in cell death kinetics between lethal compounds, compound concentrations, and cell lines. We observe that the kinetics of compound-induced cell death can be modulated by compound interactions and identify 13 compounds that induce cell death with an exceptionally rapid onset, including

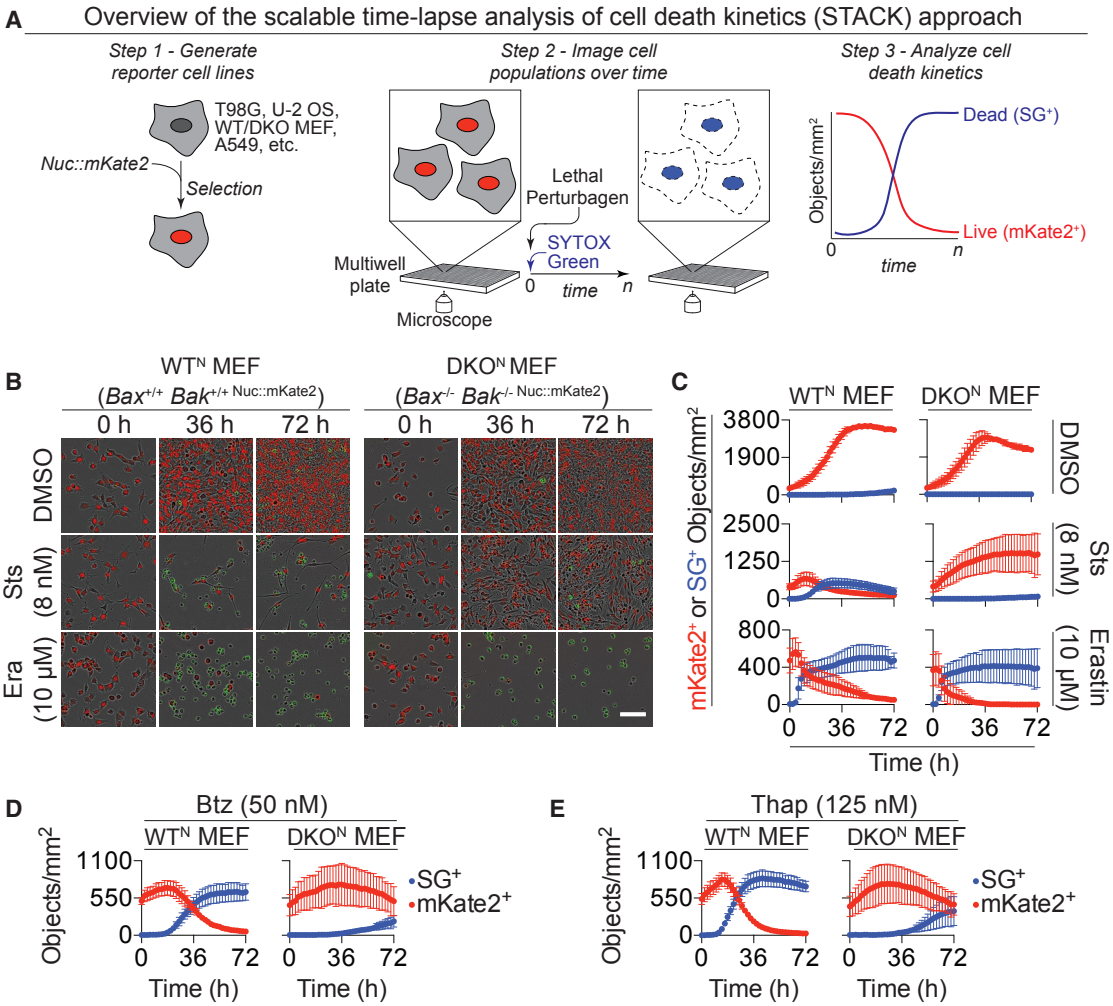

Figure 1. Measurement of Cell Death Using Live and Dead Cell Markers

(A) Overview of the STACK approach.

(B) Representative images of Nuc::mKate2-expressing *Bax*$^{+/+}$ *Bak*$^{+/+}$ (WT^{N}) and *Bax*$^{-/-}$ *Bak*$^{-/-}$ (DKO^{N}) mouse embryonic fibroblasts (MEFs) incubated with SYTOX green and treated with lethal compounds. Cells were imaged every 2 hr for 72 hr and representative images are shown for 0, 36, and 72 hr. Scale bar, 50 μm.

(C) Counts of live (mKate2^{+}) and dead (SG^{+}) cells over time for the cell lines and conditions in (B).

(D and E) Counts of mKate2^{+} and SG^{+} cells over time in response to bortezomib (Btz) and thapsigargin (Thap).

Data in (C–E) represent mean ± SD from three independent biological replicates.

the metallophore zinc pyrithione (ZP). We demonstrate that ZP triggers rapid non-apoptotic cell death via bioenergetic collapse, and the timing of cell death onset in response to ZP is determined, in part, by the metabolic flexibility of the cell. These studies help lay the foundation for the systematic, large-scale study of cell death kinetics in mammalian cell populations.

RESULTS

We developed STACK as a high-throughput method to quantify population-level cell death kinetics in large numbers of samples in parallel. STACK has three major steps: generation of "live cell" reporter cell lines, counting of live and dead cells over time, and analysis of cell death kinetics (Figure 1A). Live cells are identified by expression of nuclear-localized mKate2 (Nuc::mKate2; Artymovich and Appledorn, 2015), while dead cells are identified by uptake of the live cell-impermeant nucleic acid dye SYTOX green (SG, 20 nM), which is included in the growth medium. Nuc::mKate2 expression and incubation with SG themselves do not alter cell proliferation or sensitivity to cell death (Figures S1A and S1B). Following the addition of a lethal perturbagen, live (mKate2^{+}) and dead (SG^{+}) cells within each population are counted using an automated high-throughput microscope housed within a tissue culture incubator. As high cell density within an individual population can alter sensitivity to death-inducing stimuli (Hafner et al., 2016; Reuven et al., 2013), cells are seeded such that they are less than 50% confluent when first exposed to a lethal treatment. Phase contrast images are acquired in parallel to live and dead cell counts to assess population confluence, but this is not essential to the STACK approach.

We validated our ability to detect cell death using this approach in stable Nuc::mKate2-expressing wild-type (WT^N) and *Bax*$^{-/-}$ *Bak*$^{-/-}$ double knockout (DKO^N) mouse embryonic fibroblasts (MEFs) (Wei et al., 2001). Cells seeded in 384-well plates were treated with DMSO (vehicle control), the multikinase inhibitor staurosporine (Sts), or the system x_c^- inhibitor erastin, and imaged every 2 hr for 72 hr starting immediately after compound addition. Treatment with DMSO was not lethal to either cell line and the number of live mKate2$^+$ cells increased rapidly until plateauing around 36 hr, shortly after these populations reached ~100% confluence (Figures 1B, 1C, and S1C). Sts induces Bax/Bak-dependent apoptosis, while erastin induces Bax/Bak-independent ferroptosis (Dixon et al., 2012; Wei et al., 2001). In WT^N cells, Sts (8 nM) treatment did not immediately arrest cell proliferation. Rather, mKate2$^+$ counts increased for ~12 hr before starting to decrease, concomitant with increased SG$^+$ counts, indicative of the onset of cell death within the population (Figures 1B and 1C). DKO^N MEFs were resistant to the lethal effects of Sts treatment, as expected, although cell proliferation was slowed relative to DMSO-treated cells (Figures 1B and 1C). In both WT^N and DKO^N populations erastin (10 μM) treatment was briefly compatible with continued proliferation, but then resulted in decreased mKate2$^+$ counts and increased SG$^+$ counts (Figures 1B and 1C). Thus, using STACK we easily resolved known differences of cell death sensitivity between cell lines and lethal compounds.

Like Sts, treatment with two additional mechanistically distinct, pro-apoptotic lethal compounds, the proteasome inhibitor bortezomib (Btz) and the sarco/endoplasmic reticulum Ca^{2+}-ATPase inhibitor thapsigargin (Thap), was more lethal to WT^N than DKO^N cells, indicating that this method can capture cell death in response to diverse lethal stimuli (Figures 1D, 1E, and S1D). In these experiments few cells were simultaneously positive for both mKate2$^+$ and SG$^+$ (Figure S1E). However, SG$^+$ counts occasionally declined from the maximum (e.g., WT^N MEFs treated with Sts and Thap, Figures 1C and 1E). This phenomenon is most likely explained by the loss of SG from long-dead cells. We account for this potential confound when analyzing cell death kinetics, as described below.

A major goal was to develop metrics to summarize and quantify population cell death and cell death kinetics (Figure 1A, step 3). Toward this end, we first integrated mKate2$^+$ and SG$^+$ counts into a single metric, the lethal fraction (LF), where a value of 0 means all cells within the population are alive and a value of 1 means all cells within the population are dead (Figures 2A and S2A, STAR Methods). LF values are computed separately at each time point and therefore take into account increases in live cell population size before the onset of cell death. This calculation also includes a correction for the observed loss of SG from long-dead cells. The maximum LF score (LF_{max}) and the area under the curve (AUC) provide two useful means of summarizing in a single value the overall lethality of a treatment, but do not provide insight into cell death kinetics per se (Figure 2A).

To quantify cell death kinetics, we parameterized curves of LF scores over time using a "lag exponential death" (LED) model and extracted two key parameter values: the time lag between the addition of a lethal perturbation and the onset of cell death within a population (D_O) and the maximal cell death rate within the population (D_R) (Figures 2A and S2A) (STAR Methods). The LED model intuitively captures the typical response of cells to lethal perturbation, which involves a period of signal transduction and/or metabolic disruption prior to frank membrane permeabilization (Biton and Ashkenazi, 2011; Dixon et al., 2012; Lu et al., 2014). Sigmoidal models were also examined (Figure S2B), but had a less obvious biological interpretation and were not explored further here. In a control experiment, differences in starting cell confluence between 2% and 30% had little effect on LF scoring or the ability to fit LED curves to these data, suggesting that these methods are robust to differences in cell seeding density (Figure S2C).

We hypothesized that the intensity of a lethal stimulus and genetic background would be two key factors influencing cell death kinetics. To test this hypothesis we examined the response of WT^N and DKO^N MEFs to different concentrations of the pro-apoptotic DNA topoisomerase I inhibitor camptothecin (Cpt). For all conditions, mKate2$^+$ and SG$^+$ objects were counted every 2 hr for a total of 120 hr (Figure 2B). The resultant LF scores were visualized using what we refer to as concentration by time plots and summarized across Cpt concentrations using LF_{max} and AUC values (Figures 2C–2E). Cpt triggered substantial dose-dependent lethality in both WT^N and DKO^N MEFs, resulting in similar maximal lethality (i.e., LF_{max}) for all Cpt concentrations in both cell lines (Figure 2D). Using the LED model we fit unambiguous curves to the majority of LF scores over time and extracted D_O and D_R values (Figures 2F–2H). Simulations showed that longer time courses and higher LF_{max} values improved the confidence in the estimates of both D_O and D_R (Figure S2D), and in all experiments we excluded any LED model fits that were ambiguous (Table S1 contains summary statistics for all curve fits in this work). Increasing Cpt concentrations resulted in shorter D_O times and higher D_R rates, up to a concentration of ~1 μM, at which point cell death kinetics plateaued, albeit at different levels in WT^N versus DKO^N MEFs. For example, in response to 1.25 μM Cpt, D_O was 23 hr earlier (11 versus 34 hr) and D_R was 3.1 times faster (0.068 versus 0.022 LF/hr) in WT^N versus DKO^N MEFs. Similar results were obtained in WT^N and DKO^N MEFs treated with the DNA topoisomerase II inhibitor etoposide (Etop) (Figure S2E). Thus, Bax and Bak have an important role governing cell death kinetics in response to topoisomerase inhibition.

Of note, in these experiments we observed the highest absolute SG$^+$ counts in control (DMSO)-treated WT^N MEFs (e.g., 1831 ± 120 Obj/mm^2, mean ± SD at t = 120 hr) (Figure 2B). This was explained by: (1) the substantial proliferation that occurred in these cultures, which increased the number of live cells in the population subsequently "available" to die, and (2) the fact that these cultures quickly reached 100% confluence, which likely triggered overcrowding-induced cell death (Figures 2B and S2F). The later onset and slower maximal rate of this crowding-associated cell death was typically distinct from the earlier onset and more rapid kinetics of Cpt- or Etop-induced cell death (Figures 2G, 2H, and S2F). However, WT^N MEFs treated with 20 nM Cpt proliferated substantially before the onset of cell death (Figures 2B and S2F), and D_O and D_R values under this condition was more similar to the kinetics observed in DMSO-treated cells than to cells treated with higher concentrations of Cpt (Figures 2G and 2H). Thus, at sub-lethal compound concentrations, high cell densities and associated stresses (e.g., nutrient deprivation) may contribute to the observed cell death kinetics.

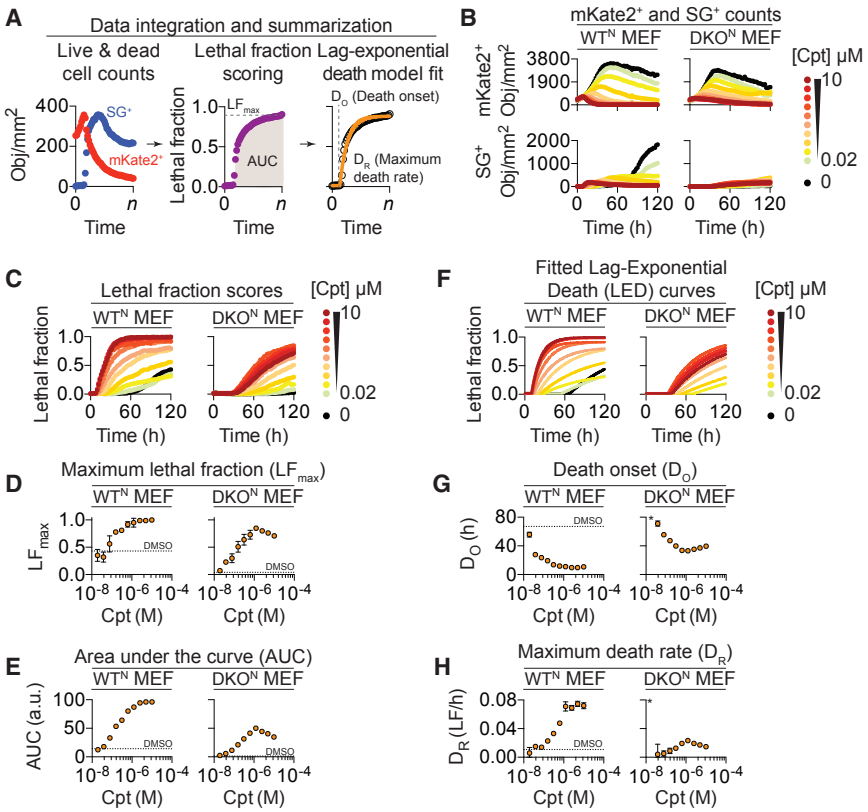

Figure 2. Quantifying Cell Death Kinetics

(A) Overview of data integration and summarization. Live and dead cell counts over time (*n*) are used to compute the lethal fraction (LF). Where appropriate, LF scores over time are parameterized using a lag exponential death (LED) model and two values are extracted: the timing of cell death onset (D_O) and the maximal cell death rate (D_R).

(B) Plots of mKate2$^+$ and SG$^+$ counts over time for WT^N and DKO^N MEFs treated with camptothecin (Cpt) or DMSO. Each colored line represents counts for a different compound concentration.

(C) LF plots computed from the data in (B).

(D and E) Maximum LF score (LF_{max}) and area under the curve (AUC) values obtained from LF curves in (C).

(F) LED curves fit to the data in (C).

(G and H) D_O and D_R parameter values for LED curves in (F). The star (*) indicates that 20 nM Cpt treatment produced ambiguous LED curve fits in DKO^N MEFs.

In (D)–(H) horizontal dotted lines indicate the average value of the vehicle (DMSO)-treated populations for comparison. LED curves could not be fit to vehicle-treated DKO^N MEFs. Results in (B–F) are the average of three independent biological replicates. For clarity, in (B, C, and F) only mean values are shown. Error bars in (D, G, and H) represent 95% confidence intervals (95% CI).

Large-Scale Analysis of Cell Death Kinetics

Cell death kinetics vary between lethal perturbations (Grootjans et al., 2016; Hafner et al., 2016; Harris et al., 2016; Tyson et al., 2012). However, the extent of this variability, whether different classes of lethal perturbations are associated with unique cell death kinetics, and the effect of genetic background on these properties, is not well understood. To investigate these questions, and explore the use of STACK in a high-throughput setting, we used STACK to profile cell death in U-2 OS osteosarcoma cells and T98G glioblastoma cells treated with 1,833 different bioactive compounds, including approved drugs, investigational anti-cancer agents, and natural products, at a fixed concentration of 5 µM (see STAR Methods and the online Data Repository for library details). These two cell lines were useful for these studies as they are genotypically distinct, suitable for imaging, and frequently used in cell death research (Forbes et al., 2011; Nakano and Vousden, 2001; Potapova et al., 2001).

Cells seeded in 384-well plates were exposed to library compounds and imaged every 2 hr for 118 hr (U-2 OS^N) or every 4 hr for 96 hr (T98G^N). High quality data were obtained for 1,885 conditions in U-2 OS^N cells (79 DMSO-negative controls, 1,806 test compounds) and 1,906 conditions (87 DMSO-negative controls, 1,819 test compounds) in T98G^N cells (see online Data Repository for all live and dead cell counts from both experiments). Most tested compounds were not lethal to either cell line; plate-based LF_{max} thresholds and an absolute minimum LF_{max} cutoff of 0.5 (see STAR Methods) were used to identify 140 high-confidence lethal compounds in U-2 OS^N and a partially overlapping set of 140 high-confidence lethal compounds in T98G^N cells (Figure 3A and Table S2). Unambiguous LED model fits were obtained for 139/140 compounds from U-2 OS^N cells and 136/140 compounds from T98G^N cells. Manual inspection indicated that three compounds with ambiguous fits in T98G^N cells (elaiophylin, BGT226, and dioscin) initiated cell death immediately upon compound addition. These compounds were therefore assigned D_O values = 1 hr, and ultimately included in a set of 79 high-confidence lethal compounds common to both cell lines (Figure 3A and Table S2). These structurally and mechanistically diverse compounds provided a useful test set with which to explore how cell death kinetics varied by compound, compound class, and cell line.

The 79 common high-confidence lethal compounds triggered cell death with similar overall potency (i.e., LF_{max}) in both U-2 OS^N and T98G^N cells (Figures S3A and S3B). However, the kinetics of cell death induced by these compounds varied greatly in both U-2 OS^N cells (ranges, D_O = 1–73 hr; D_R = 0.005–1.4 LF/hr) and T98G^N cells (ranges, D_O = 1–55 hr; D_R = 0.013–0.2 LF/hr). D_O times for individual compounds were correlated between U-2 OS^N and T98G^N cells (Spearman $r = 0.48$, $p < 0.0001$), suggesting that the timing of cell death onset was largely dictated by the lethal mechanism of action of each compound (Figure 3B). Conversely, D_R rates for individual compounds were not correlated between U-2 OS^N and T98G^N cells (Spearman $r = 0.04$, $p > 0.05$), indicating that for a given lethal compound the maximal rate of cell death was highly influenced by genetic background (Figure 3B). D_O and D_R were negatively correlated in both cell lines (U-2 OS^N = −0.43, T98G^N = −0.54, $p < 0.001$ for both comparisons), indicating that, in both U-2

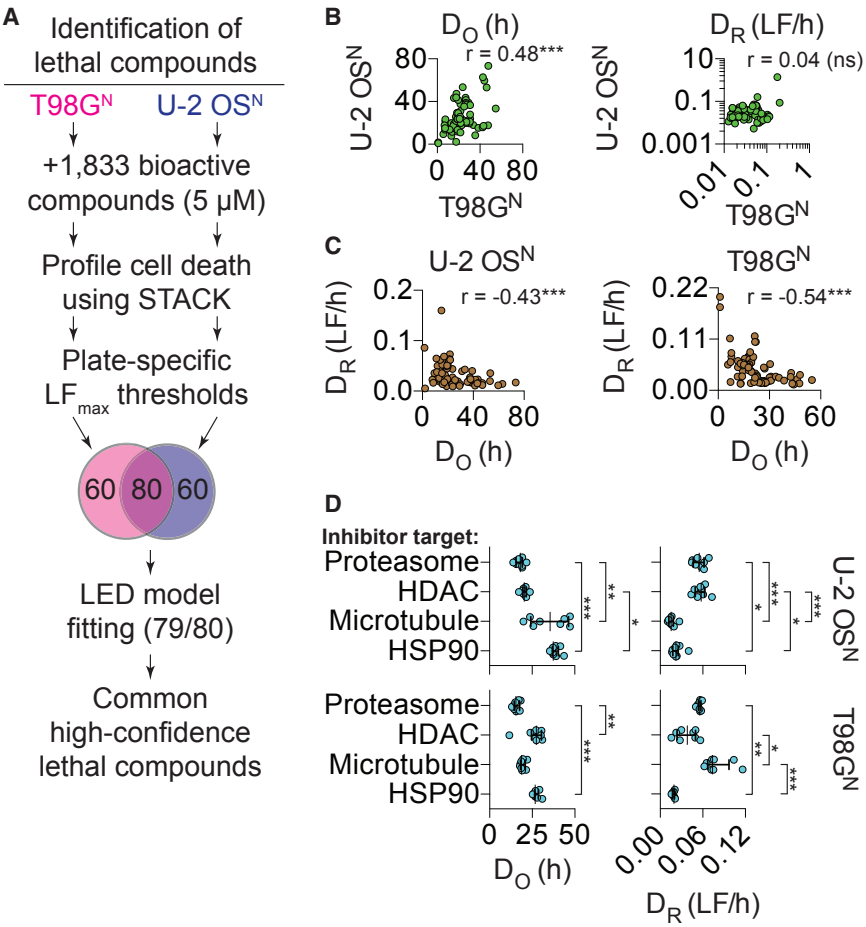

Figure 3. Large-Scale Comparative Analysis of Cell Death Kinetics

(A) Parallel bioactive compound screens in U-2 OS^N and T98G^N cell lines identify 79 common high-confidence lethal compounds.

(B) D_O and D_R in T98G^N versus U-2 OS^N cells for the 79 common high-confidence lethal compounds.

(C) D_O versus D_R in T98G^N and U-2 OS^N cells for the 79 common high-confidence lethal compounds. In (B) and (C), Spearman r correlation values are shown.

(D) D_O and D_R for common high-confidence lethal compounds that target the proteasome (n = 8), histone deacetylases (HDAC, n = 8), microtubules (n = 8), or heat shock protein 90 (HSP90, n = 9). Bars and lines indicate median with interquartile range. Statistical significance was assessed using the Mann-Whitney U test.

In (B)–(D) each dot represents a single compound and ***p < 0.001, **p < 0.01, *p < 0.05; ns, not significant.

OS^N and T98G^N cells, when cell death onset is later it tends to occurs with a lower maximal rate (Figure 3C).

We investigated in greater detail whether cell death kinetics varied for a set of highly lethal compounds. For this comparison we focused on compounds from four highly lethal (i.e., median LF_{max} > 0.7) compound classes: proteasome inhibitors (n = 8), heat shock protein 90 (HSP90) inhibitors (n = 9), histone deacetylase (HDAC) inhibitors (n = 8), and tubulin/microtubule inhibitors (n = 8). Compounds from each class tended to cluster together with characteristic D_O and D_R values that, nonetheless, varied significantly between compound class and cell line (Figure 3D). For example, in both cell lines, proteasome inhibitors triggered cell death with a significantly shorter median D_O (U-2 OS^N = 18 hr, T98G^N = 15 hr) and higher median D_R (U-2 OS^N D_R = 0.055 LF/hr, T98G^N D_R = 0.054 LF/hr) than HSP90 inhibitors (D_O U-2 OS^N = 37 hr, T98G^N = 27 hr; D_R U-2 OS^N = 0.022 LF/hr, T98G^N = 0.019 LF/hr) (Kruskal-Wallis H test with Dunn's multiple comparisons tests, p < 0.05 for all comparisons) in both cell lines. By contrast, proteasome inhibitors triggered cell death with shorter D_O than HDAC inhibitors in T98G^N cells (Mann-Whitney U test, both p < 0.01) but not U-2 OS^N cells (Mann-Whitney U test, both p > 0.05). In a final example, for microtubule inhibitors, median D_O was significantly longer and median D_R significantly lower in U-2 OS^N cells (D_O = 36 hr, D_R = 0.015 LF/hr) compared with T98G^N cells (D_O = 19 hr, D_R = 0.074 LF/hr) (Mann-Whitney U test, both p < 0.001). These and other significant differences indicate that lethal compounds trigger cell death with compound-specific and cell line-specific kinetics that can be readily distinguished using STACK.

Compound Interactions Alter Cell Death Kinetics

Sometimes the combination of two compounds can produce a cell death phenotype that deviates significantly from expectations based on the known effects of each individual compound (Lehár et al., 2008). We reasoned that compound interactions might be reflected in changes in cell death or cell death kinetics detectable using STACK. As a case study, we investigated in T98G^N cells how a sub-lethal concentration of the alkylating agent temozolomide (TMZ, 400 μM) modulated cell death induced by our library of 1,833 bioactive compounds (Figure 4A). As above, cell death profiles were acquired using STACK, and the results compared with the previous dataset obtained with this library in T98G^N cells in the absence of TMZ. As the lethality of a given compound could be modulated substantially by TMZ, this precluded the use of LED curve fits. We therefore searched for interactions across all 1,833 compounds using AUC and LF_{max} values derived directly from LF scores over time. Computing the expected effect of compound combinations is not trivial and there is no consensus about the best method to employ (Fitzgerald et al., 2006; Lehár et al., 2008). We therefore modeled the expected effect of each drug combination with a simple additive model, using the experimentally observed AUC or LF_{max} values for each treatment alone as input (Figure 4A; Table S3) (see STAR Methods). Other metrics of cell death or models of compound interaction (e.g., multiplicative models) may yield alternative predictions of enhancing or suppressive interactions but were not explored here.

Significant compound interactions were identified using two methods. First, we used the behavior of the control treatments (Figure 4B, black dots) to establish conservative thresholds

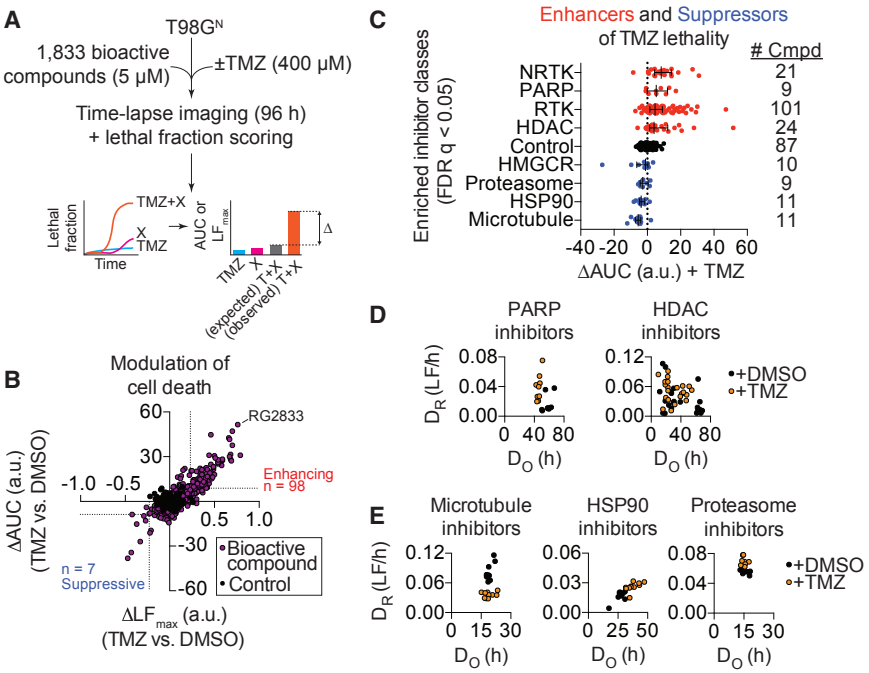

Figure 4. Identifying and Quantifying Compound Interactions

(A) T98G^N cells treated with 1,833 bioactive compounds (5 μM) ± temozolomide (TMZ, 400 μM) were imaged every 4 hr for 96 hr. Lethal fraction scores were computed, and AUC and LF_{max} values for TMZ (T) alone, and each library compound (X) alone, were used to compute the expected AUC or LF_{max} for each combination, using an additive model. Deviations (Δ) between the expected and observed AUC or LF_{max} values were then computed.

(B) ΔLF_{max} versus ΔAUC values for 1,819 compounds that passed quality control measures. Enhancing (n = 98) and suppressive (n = 7) interactions were identified using statistical thresholds (dotted lines) for significant deviation between expected and observed effects. A known enhancing interaction between TMZ and RG2833 is highlighted.

(C) Compound classes exhibiting significant interaction with TMZ identified using compound set enrichment analysis (false discovery rate [FDR] q < 0.05). The number of compounds (# Cmpd) within each class is indicated at right. NRTK, non-receptor tyrosine kinase; PARP, poly (ADP) ribose polymerase; RTK, receptor tyrosine kinase; HDAC, histone deacetylase; HMGCR, 3-hydroxy-3-methylglutaryl-CoA reductase; HSP90, heat shock protein 90.

(D and E) Plots of D_O versus D_R for select lethal compound classes ± TMZ. Each dot represents a single compound for which suitable LED curve fits could be obtained ± TMZ. The number of compounds are: PARP inhibitors (n = 9), HDAC inhibitors (n = 22), microtubule inhibitors (n = 9), proteasome inhibitors (n = 8), and HSP90 inhibitors (n = 10). In (D) and (E) results with +DMSO are the same as those presented in Figure 3D.

(|ΔAUC| > 8.8, $|\Delta LF_{max}|$ > 0.23) for significant enhancer and suppressor interactions (see STAR Methods). This analysis identified 98 enhancing interactions, including known interactions between TMZ and the HDAC inhibitor RG2833/RGFP109 (ΔAUC = 52, ΔLF_{max} = 0.76) and the dual mechanistic target of rapamycin (mTOR)/phosphatidylinositol 3-kinase (PI3K) inhibitor BEZ235 (ΔAUC = 9.7, ΔLF_{max} = 0.27) (Li et al., 2016; Yu et al., 2015) (Figure 4B). Second, we used ΔAUC values and compound set enrichment analysis (Liu et al., 2013) to identify compound classes significantly modulated by TMZ. This analysis identified four compound classes for which the lethality was significantly enhanced by TMZ (false discovery rate q < 0.05): non-receptor tyrosine kinase inhibitors, poly (ADP-ribose) polymerase (PARP) inhibitors, receptor tyrosine kinase (RTK) inhibitors, and HDAC inhibitors (Figure 4C). PARP and HDAC inhibitors are known enhancers of TMZ-induced death (Gojo et al., 2016; Lee et al., 2012), providing further confidence that the methods employed here can recover true compound interactions. For two compound classes we obtained unambiguous LED fits for a suitable number of compounds both with and without TMZ, enabling a direct assessment of the effect of TMZ on cell death kinetics. For PARP inhibitors (n = 9), the addition of TMZ significantly shortened median D_O and significantly increased median D_R (Mann-Whitney U test, p < 0.01 for both comparisons), while for HDAC inhibitors (n = 22) TMZ had no effect on D_O but significantly increased D_R (Mann-Whitney U test, p < 0.01) (Figure 4E).

In addition to the above enhancing interactions, we identified apparent suppressive interactions between TMZ and four compound classes: microtubule inhibitors, HSP90 inhibitors, proteasome inhibitors, and 3-hydroxy-3-methylglutaryl-CoA reductase inhibitors (Figure 4C). In the presence of TMZ, D_R was significantly lower for microtubule inhibitors and D_O significantly lengthened for HSP90 inhibitors (Mann-Whitney U test, p < 0.001 for both comparisons) (Figure 4E). TMZ actually increased D_R when combined with proteasome inhibitors (Figure 4E), and in this case the detection of an apparent suppressive interaction is best explained by the fact that proteasome inhibitors were already maximally lethal alone ($LF_{max} \sim 1$) and lethality could not be further enhanced by TMZ (Figure S4). These results indicate that compound interactions modify cell death kinetics in a compound class-specific manner that can be detected using STACK.

Identification and Analysis of Rapid-Onset Lethal Compounds

Cell death kinetics could provide a means of classifying compound activity that is complementary to traditional dose-dependent metrics and help identify lethal compounds with unusual mechanisms of action. To explore this concept, we ordered all high-confidence lethal compounds (U-2 OS^N, n = 80; T98G^N, n = 79) by D_O and empirically defined 13 compounds in the lowest 25th percentile ($D_O \leq$ 15.7 hr in U-2 OS^N, $D_O \leq$ 15.6 hr in T98G^N) as rapid-onset lethals (ROLs), as well as seven compounds in the highest 75th percentile (D_O > 35.3 hr in U-2 OS^N, D_O > 27.3 hr in T98G^N) as slow onset lethals (Figure 5A; Table S4). For the remainder of this work we focused on the ROL compounds.

ROL compounds included three proteasome inhibitors (carfilzomib, Btz, and MG132), but otherwise lacked common structural features or canonical targets (Figures 5B and 5C). Several

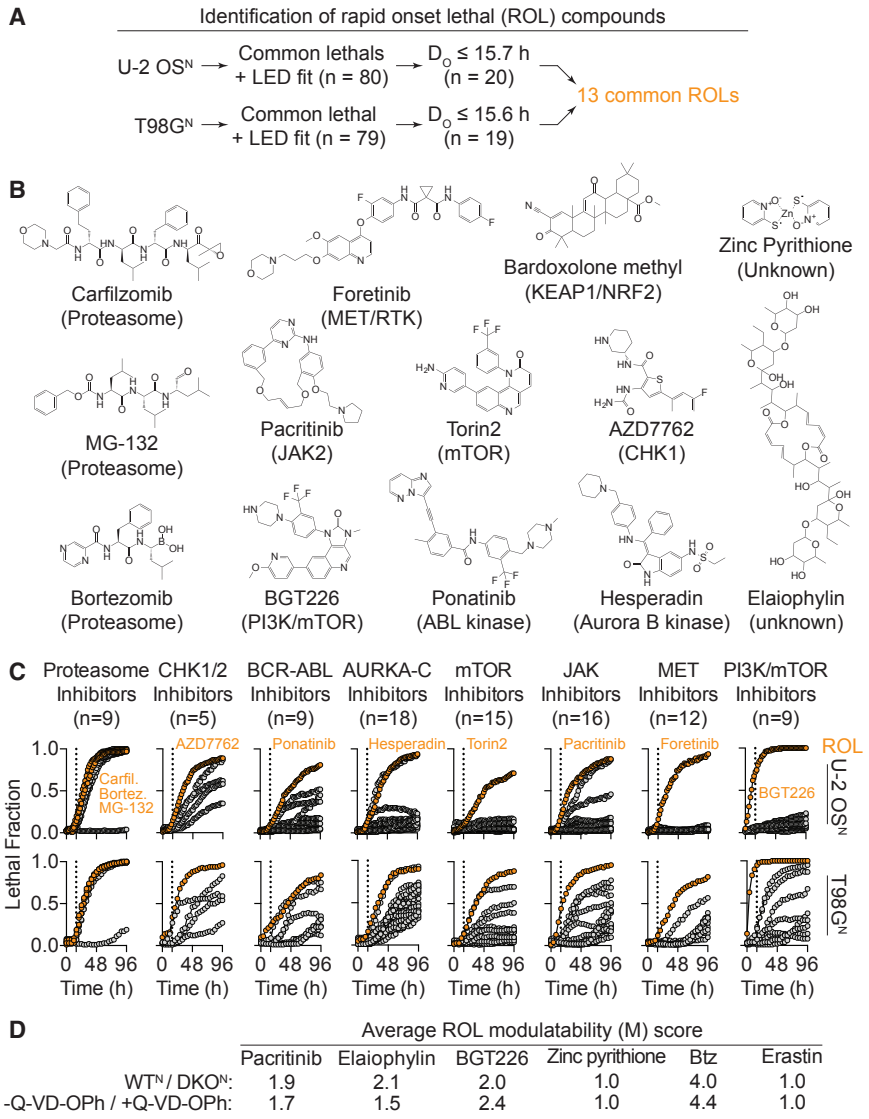

Figure 5. Identifying Rapid-Onset Lethal Compounds

(A) 13 rapid-onset lethal (ROL) compounds defined empirically as those compounds within the lowest 25th percentile for D_O values from the sets of high-confidence lethal compounds identified in U-2 OS^N and T98G^N.

(B) Structures of the 13 ROL compounds. Putative primary targets are in parentheses. Note: kinase inhibitors typically have >1 target in cells.

(C) LF scores over time for each ROL compound (colored orange) compared with other tested compounds in the same putative target class (colored gray). The vertical dotted lines indicate the cell line-specific D_O 25th percentile ROL cutoffs.

(D) Median modulatability (M) score of cell death in WT^N versus DKO^N MEFs (WT^N/DKO^N) induced by the indicated ROL compounds and controls, each tested across a 10-point, 2-fold dilution series. Modulatability was also assessed at a single lethal concentration ± Q-VD-OPh. Results in (D) are from three independent biological replicates.

ROL compounds were members of larger compound classes that shared the same putative protein target(s) yet exhibited distinct cell death kinetic profiles. For example, BGT226 was the only dual PI3K/mTOR inhibitor (n = 9) that was lethal in U-2 OS^N cells (Figure 5C). Likewise the mTOR inhibitor Torin2, the JAK inhibitor pacritinib, and the RTK inhibitor foretinib caused greater or more rapid cell death than other members from the same putative target class in one or both cell lines (Figure 5C). Protein kinase inhibitors are rarely specific (Anastassiadis et al., 2011; Taipale et al., 2013) and we infer that these compounds trigger a ROL phenotype by engaging unconventional targets or mechanisms.

The ROL phenotype could result from rapid activation of a specific cell death pathway, direct physical disruption of the plasma membrane or potentially other mechanisms (Palchaudhuri et al., 2015; Wolpaw et al., 2011). To begin to distinguish between these possibilities, we studied four ROL compounds, BGT226, pacritinib, the natural product macrolide antibiotic elaiophylin, and the metallophore ZP, in WT^N and DKO^N MEFs. Each compound was tested in a 10-point, 2-fold dose-response series and the ratio of STACK-derived AUC values in WT^N versus DKO^N MEFs was used to define a modulatability (M) score. M scores >1 indicated the induction of Bax/Bak-dependent apoptosis, while M scores ≈1 indicated Bax/Bak-independent cell death. Treatment with high concentrations of pacritinib (20 μM), elaiophylin (≥10 μM), and BGT226 (≥5 μM) was associated with the near-instantaneous induction of cell death upon compound addition and M scores near 1 (Figures S5A and S5B). However, median M scores across all concentrations indicated that pacritinib (M = 1.9), elaiophylin (M = 2.1), and BGT226 (M = 2.0) triggered Bax/Bak-dependent apoptosis at lower concentrations (Figure 5D). Unlike these compounds, ZP-induced cell death was not modulated at any concentration by the deletion of Bax and Bak (M = 1.0) (Figures 5D, S5A, and S5B). Likewise, ZP-induced death was not modulated by co-treatment with the pan-caspase inhibitor Q-VD-OPh (25 μM) (M = 1.0) (Figure 5D). Unlike elaiophylin and BGT226, ZP triggered cell death with a clear delay in human cancer cell lines (Figure S5C), inconsistent with direct membrane permeabilization. Rather, these observations suggested that ZP triggered rapid-onset cell death through a specific biochemical mechanism.

We investigated further the mechanism of ZP-induced rapid-onset lethality. These studies were performed in human T98G^N and A549^N cancer cells that, compared with MEFs, exhibited a more substantial delay in cell death onset, which facilitated functional studies (Figure 6A). Using inductively coupled plasma mass spectrometry we found that ZP treatment increased intracellular elemental Zn levels in both cell lines, in a manner that was sensitive to the zinc chelator diethylenetriaminepentaacetic acid

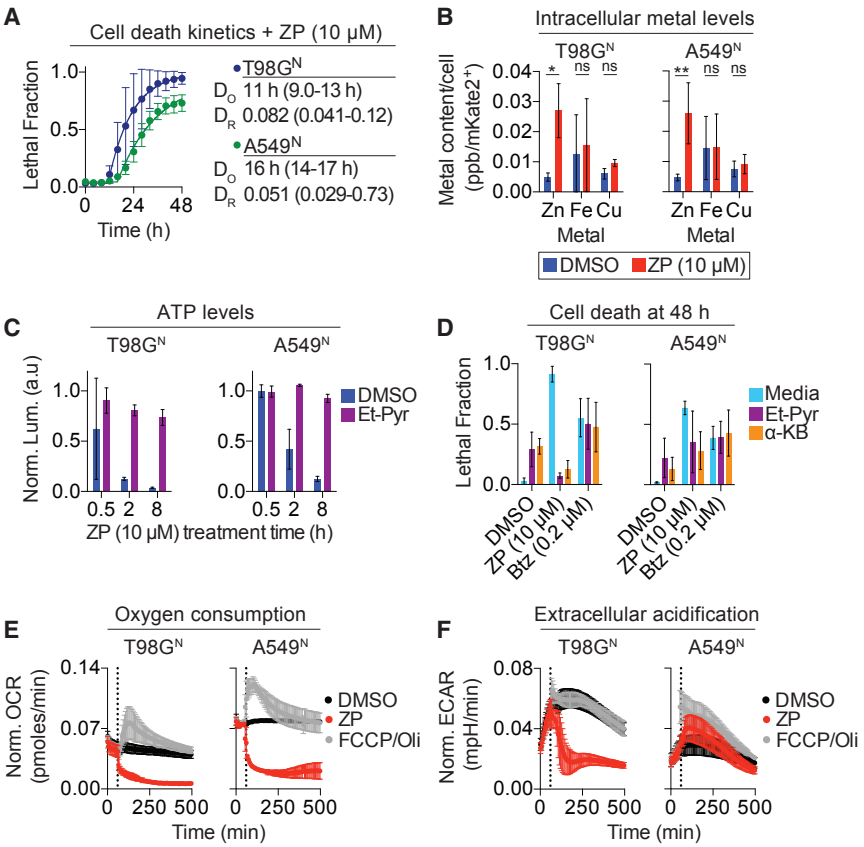

Figure 6. Differences in Basal Energy Metabolism Explain Differences in D_O

(A) Cell death kinetics in T98G^N and A549^N cells in response to zinc pyrithione (ZP). Lethal fraction scores and LED curves are plotted.

(B) Intracellular Zn, Fe, and Cu levels measured using inductively coupled plasma mass spectrometry following ZP treatment (10 μM, 2 hr). *p < 0.05, **p < 0.01; ns, not significant; two-way ANOVA with Sidak multiple comparison tests.

(C) ATP levels over time + ZP (10 μM) ± ethyl pyruvate (Et-Pyr). All results are normalized to DMSO-treated controls at t = 0 hr.

(D) Lethal fraction at 48 hr in T98G^N and A549^N cells treated with ZP or Btz ± Et-Pyr or α-ketobutyrate (α-KB).

(E and F) Measurement of oxygen consumption rate (OCR) (E) and extracellular acidification rate (ECAR) (F) using Seahorse technology. Treatments were DMSO, ZP (10 μM), or carbonyl cyanide-4-(trifluoromethoxy)phenylhydrazone (FCCP, 2 μM) + oligomycin (Oli, 1 μM). The vertical dotted line indicates the time (60 min) of compound injection. OCR and ECAR are normalized to mKate2$^+$ counts at the start of the experiment.

Data represent mean ± SD from four or five (A), three (B, E, and F), or four to six (C and D) independent biological replicates.

(DTPA), without affecting the levels of other metals (Fe, Cu) (Figures 6B and S6A). DTPA also specifically inhibited ZP-induced cell death in both cell lines, without affecting cell death induced by Btz or the improved erastin analog erastin2 (Figures S6A and S6B). Consistent with results obtained in MEFs, a pan-caspase inhibitor (Q-VD-OPh) had no ability to block ZP-induced cell death in either cell line, and a ferroptosis-specific inhibitor (ferrostatin-1) was likewise ineffective (Figures S6B). Thus, in both T98G^N and A549^N cells, ZP treatment specifically increases intracellular Zn leading to caspase-independent cell death through a pathway distinct from ferroptosis.

Zn overload is reported to disrupt cellular bioenergetics and deplete ATP (Carraway and Dobner, 2012; Dineley et al., 2003; Kelland et al., 2004; Lamore et al., 2010; Sheline et al., 2000). Indeed, ZP treatment resulted in rapid ATP depletion in both T98G^N and A549^N cells, a response not observed in response to Btz or Era2 (Figures 6C and S6C). ZP-induced ATP depletion and cell death were prevented by the addition of ethyl pyruvate (20 mM) or alpha-ketobutyrate (20 mM) (Figures 6C and 6D), compounds that can act as electron acceptors to promote cytosolic regeneration of nicotinamide adenine dinucleotide (NAD$^+$) from NADH by lactate dehydrogenase (Sullivan et al., 2015). NAD$^+$ is essential for glycolytic ATP synthesis and these results suggested that a defect in glycolysis could be responsible for rapid ATP depletion and cell death following ZP treatment. Using Seahorse technology we observed that ZP treatment (10 μM) caused an immediate drop in the oxygen consumption rate, and a delayed inhibition of extracellular acidification (ECAR), a measure of glycolysis, in both cell lines (Figures 6E and 6F). We noted that ECAR was inhibited more rapidly in T98G^N versus A549^N cells. This suggested that T98G^N cells were less able to mobilize spare glycolytic capacity in response to the inhibition of oxidative phosphorylation (OXPHOS) than A549^N cells. Indeed, treatment with a combination of carbonyl cyanide-4-(trifluoromethoxy)phenylhydrazone and oligomycin to maximally stimulate glycolysis substantially elevated ECAR in A549^N but not T98G^N cells (Figure 6F). Thus, T98G^N cells are likely less able to adapt to inhibition of OXPHOS with a compensatory increase in glycolysis, deplete ATP more quickly, and die with an earlier onset compared with A549^N cells (Figures 6A and 6C). Ultimately, however, both T98G^N and A549^N cells succumb quickly to the combined inhibition of OXPHOS and glycolysis.

DISCUSSION

We developed STACK as a large-scale method to quantify cell death kinetics in mammalian cell populations. STACK integrates counts of both live (mKate2$^+$) and dead (SG$^+$) cells into a single kinetic curve that can be parameterized using the LED model. Cell death kinetics can then be minimally summarized using two key parameters, D_O and D_R. Using STACK we have quantified the kinetics of apoptotic and non-apoptotic cell death induced by diverse lethal stresses in multiple cell lines. This method therefore appears to be highly generalizable and, when combined with high-throughput microscopy, can be used to examine cell death kinetics for over 1,800 different

conditions in a single experiment. We envision that STACK will be highly complementary to other recently developed kinetic approaches to measuring cell viability (Hafner et al., 2016; Harris et al., 2016; Tyson et al., 2012).

Compounds with similar overall maximum lethality (i.e., LF_{max}) exhibited significant variation in D_O and D_R. For example, multiple proteasome inhibitors, HDAC inhibitors, microtubule inhibitors, and HSP90 inhibitors tended to cluster around distinct, characteristic D_O and D_R values. The observed clustering was independent of compound structure and observed despite the fact that each compound was tested at a single concentration (5 μM). Our observations suggest that the kinetics of lethal compound-induced cell death are fundamentally constrained: D_O cannot be reduced below a certain minimum threshold, while D_R cannot be increased above a certain maximum limit, no matter how much compound is employed or how potent a compound may be, as defined by traditional dose-based metrics.

D_O and D_R quantify cell death kinetics at the population level. A goal of ongoing and future work is to explain the observed differences in D_O and D_R between lethal compounds and cell lines at the cellular and molecular levels. D_O captures the average length of time between the addition of a lethal perturbagen and the initial onset of widespread membrane permeabilization within the population. Factors that contribute to D_O likely include the rates of compound uptake and metabolism, the extent of target engagement, the time required following target engagement to deplete essential metabolites below a minimum threshold or accumulate stress to lethal levels, and the time needed to transduce a pro-death signal to the cell death execution machinery. D_R expresses the variability in cell death onset between individual cells within a population. These differences, which reflect cell-to-cell variability in lethal compound activity, may be due to differences in the metabolic state, cell-cycle phase, gene expression, or signaling pathway activity of individual cells at the time of compound addition (Fallahi-Sichani et al., 2013; Paek et al., 2016; Roux et al., 2015; Sarosiek et al., 2013; Sharma et al., 2010; Spencer et al., 2009; Thorburn et al., 2014). One prediction is that cell death mechanisms with relatively few regulatory inputs will result in cell death with a high D_R relative to mechanisms with more layers of regulation.

Using STACK we empirically defined a set of compounds that induced rapid-onset lethality. At high concentrations, certain compounds (e.g., elaiophylin, BGT226) triggered near-instantaneous cell death, most consistent with direct plasma membrane permeabilization (Wolpaw et al., 2011). By contrast, ZP triggered a ROL phenotype via rapid ATP depletion and the induction of non-apoptotic cell death. Non-apoptotic cell death was not, however, synonymous with the ROL phenotype. Proteasome inhibitors such as Btz induce rapid-onset lethality but, unlike zinc overload, trigger classic Bax/Bak-dependent apoptotic cell death (e.g., Figure 1D). The specific mechanism linking proteasome inhibition to the initiation of apoptosis may involve the depletion of intracellular amino acid pools (Suraweera et al., 2012). Thus, the rapid depletion of essential metabolites, such as ATP or amino acids, could be a common mechanism that triggers rapid-onset lethality.

By directly counting both live and dead cells STACK overcomes technical artifacts associated with indirect assays of cell viability that measure population metabolic activity, which can be altered by compound treatment independent of changes in live cell number (Chan et al., 2013). However, unusual nuclear morphologies, prolonged nuclear retention of mKate2 in dead cells, or extremely rapid loss of SG from dead cells, could confound the detection of live and dead cells. Careful optimization of image analysis routines is essential to the success of this method. Currently, the analysis of cell death using STACK is optimized for adherent, sub-confluent cell populations. Quantifying the kinetics of cell death in non-adherent cells or in fully confluent cultures will require further technical developments. These developments will expand the range of conditions where STACK can be used to quantify mammalian population cell death kinetics.

STAR★METHODS

Detailed methods are provided in the online version of this paper and include the following:

- KEY RESOURCES TABLE
- CONTACT FOR REAGENT AND RESOURCE SHARING
- EXPERIMENTAL MODEL AND SUBJECT DETAILS
  - Cell Lines
- METHOD DETAILS
  - Nuc::mKate2-Expressing Cell Lines
  - Cell Seeding and Compound Addition
  - Measurement of Cell Viability with PrestoBlue
  - STACK Data Acquisition and Analysis
  - Bioactive Compound Profiling and Analysis
  - Analysis of ROL Cell Death Modulatability
  - Seahorse Assay
  - Measurements of Intracellular Metal Levels
  - Measurement of ATP Levels
- QUANTIFICATION AND STATISTICAL ANALYSIS
- DATA AVAILABILITY

SUPPLEMENTAL INFORMATION

Supplemental Information includes six figures and four tables and can be found with this article online at http://dx.doi.org/10.1016/j.cels.2017.05.002.

AUTHOR CONTRIBUTIONS

G.C.F., M.C., and S.J.D. designed the experiments. G.C.F., A.W., J.Y.C., and S.J.D. collected and analyzed data. G.C.F. and S.J.D. wrote the paper.

ACKNOWLEDGMENTS

We thank Marisa Hom and Zintis Inde for help with experiments, Sohiel Memarsadeghi for advice on microscopy, and David Clarke and members of the Dixon lab for comments on the manuscript. This work was supported by the NIH (4R00CA166517-03) and a Damon Runyon-Rachleff Innovation award to S.J.D.

Received: October 26, 2016
Revised: February 6, 2017
Accepted: May 8, 2017
Published: June 7, 2017

REFERENCES

Anastassiadis, T., Deacon, S.W., Devarajan, K., Ma, H., and Peterson, J.R. (2011). Comprehensive assay of kinase catalytic activity reveals features of kinase inhibitor selectivity. Nat. Biotechnol. *29*, 1039–1045.

Artymovich, K., and Appledorn, D.M. (2015). A multiplexed method for kinetic measurements of apoptosis and proliferation using live-content imaging. Methods Mol. Biol. *1219*, 35–42.

Bernheim, J.L., Mendelsohn, J., Kelley, M.F., and Dorian, R. (1977). Kinetics of cell death and disintegration in human lymphocyte cultures. Proc. Natl. Acad. Sci. USA *74*, 2536–2540.

Biton, S., and Ashkenazi, A. (2011). NEMO and RIP1 control cell fate in response to extensive DNA damage via TNF-α feedforward signaling. Cell *145*, 92–103.

Carraway, R.E., and Dobner, P.R. (2012). Zinc pyrithione induces ERK- and PKC-dependent necrosis distinct from TPEN-induced apoptosis in prostate cancer cells. Biochim. Biophys. Acta *1823*, 544–557.

Chan, G.K.Y., Kleinheinz, T.L., Peterson, D., and Moffat, J.G. (2013). A simple high-content cell cycle assay reveals frequent discrepancies between cell number and ATP and MTS proliferation assays. PLoS One *8*, e63583.

Dineley, K.E., Votyakova, T.V., and Reynolds, I.J. (2003). Zinc inhibition of cellular energy production: implications for mitochondria and neurodegeneration. J. Neurochem. *85*, 563–570.

Dixon, S.J., Lemberg, K.M., Lamprecht, M.R., Skouta, R., Zaitsev, E.M., Gleason, C.E., Patel, D.N., Bauer, A.J., Cantley, A.M., Yang, W.S., et al. (2012). Ferroptosis: an iron-dependent form of nonapoptotic cell death. Cell *149*, 1060–1072.

Dixon, S.J., Patel, D.N., Welsch, M., Skouta, R., Lee, E.D., Hayano, M., Thomas, A.G., Gleason, C.E., Tatonetti, N.P., Slusher, B.S., et al. (2014). Pharmacological inhibition of cystine-glutamate exchange induces endoplasmic reticulum stress and ferroptosis. Elife *3*, e02523.

Faleiro, L., and Lazebnik, Y. (2000). Caspases disrupt the nuclear-cytoplasmic barrier. J. Cell Biol. *151*, 951–959.

Fallahi-Sichani, M., Honarnejad, S., Heiser, L.M., Gray, J.W., and Sorger, P.K. (2013). Metrics other than potency reveal systematic variation in responses to cancer drugs. Nat. Chem. Biol. *9*, 708–714.

Fitzgerald, J.B., Schoeberl, B., Nielsen, U.B., and Sorger, P.K. (2006). Systems biology and combination therapy in the quest for clinical efficacy. Nat. Chem. Biol. *2*, 458–466.

Forbes, S.A., Bindal, N., Bamford, S., Cole, C., Kok, C.Y., Beare, D., Jia, M., Shepherd, R., Leung, K., Menzies, A., et al. (2011). COSMIC: mining complete cancer genomes in the Catalogue of Somatic Mutations in Cancer. Nucleic Acids Res. *39*, D945–D950.

Gojo, I., Beumer, J.H., Pratz, K.W., McDevitt, M.A., Baer, M.R., Blackford, A.L., Smith, B.D., Gore, S.D., Carraway, H., Showel, M.M., et al. (2016). A phase 1 study of the PARP inhibitor veliparib in combination with temozolomide in acute myeloid leukemia. Clin. Cancer Res. *23*, 697–706.

Gong, Y.-N., Guy, C., Olauson, H., Becker, J.U., Yang, M., Fitzgerald, P., Linkermann, A., and Green, D.R. (2017). ESCRT-III acts downstream of MLKL to regulate necroptotic cell death and its consequences. Cell *169*, 286–300.e16.

Grootjans, S., Hassannia, B., Delrue, I., Goossens, V., Wiernicki, B., Dondelinger, Y., Bertrand, M.J.M., Krysko, D.V., Vuylsteke, M., Vandenabeele, P., and Vanden Berghe, T. (2016). A real-time fluorometric method for the simultaneous detection of cell death type and rate. Nat. Protoc. *11*, 1444–1454.

Hafner, M., Niepel, M., Chung, M., and Sorger, P.K. (2016). Growth rate inhibition metrics correct for confounders in measuring sensitivity to cancer drugs. Nat. Methods *13*, 521–527.

Harris, L.A., Frick, P.L., Garbett, S.P., Hardeman, K.N., Paudel, B.B., Lopez, C.F., Quaranta, V., and Tyson, D.R. (2016). An unbiased metric of antiproliferative drug effect in vitro. Nat. Methods *13*, 497–500.

Haverty, P.M., Lin, E., Tan, J., Yu, Y., Lam, B., Lianoglou, S., Neve, R.M., Martin, S., Settleman, J., Yauch, R.L., and Bourgon, R. (2016). Reproducible pharmacogenomic profiling of cancer cell line panels. Nature *533*, 333–337.

Kelland, E.E., Kelly, M.D., and Toms, N.J. (2004). Pyruvate limits zinc-induced rat oligodendrocyte progenitor cell death. Eur. J. Neurosci. *19*, 287–294.

Kihlmark, M., Rustum, C., Eriksson, C., Beckman, M., Iverfeldt, K., and Hallberg, E. (2004). Correlation between nucleocytoplasmic transport and caspase-3-dependent dismantling of nuclear pores during apoptosis. Exp. Cell Res. *293*, 346–356.

Lamore, S.D., Cabello, C.M., and Wondrak, G.T. (2010). The topical antimicrobial zinc pyrithione is a heat shock response inducer that causes DNA damage and PARP-dependent energy crisis in human skin cells. Cell Stress Chaperones *15*, 309–322.

Lee, E.Q., Puduvalli, V.K., Reid, J.M., Kuhn, J.G., Lamborn, K.R., Cloughesy, T.F., Chang, S.M., Drappatz, J., Yung, W.K.A., Gilbert, M.R., et al. (2012). Phase I study of vorinostat in combination with temozolomide in patients with high-grade gliomas: North American Brain Tumor Consortium Study 04-03. Clin. Cancer Res. *18*, 6032–6039.

Lehár, J., Stockwell, B.R., Giaever, G., and Nislow, C. (2008). Combination chemical genetics. Nat. Chem. Biol. *4*, 674–681.

Li, Z.-Y., Li, Q.-Z., Chen, L., Chen, B.-D., Wang, B., Zhang, X.-J., and Li, W.-P. (2016). Histone deacetylase inhibitor RGFP109 overcomes temozolomide resistance by blocking NF-κB-dependent transcription in glioblastoma cell lines. Neurochem. Res. *41*, 3192–3205.

Liu, Y., Shoji-Kawata, S., Sumpter, R.M., Wei, Y., Ginet, V., Zhang, L., Posner, B., Tran, K.A., Green, D.R., Xavier, R.J., et al. (2013). Autosis is a Na+,K+-ATPase-regulated form of cell death triggered by autophagy-inducing peptides, starvation, and hypoxia-ischemia. Proc. Natl. Acad. Sci. USA *110*, 20364–20371.

Lu, M., Lawrence, D.A., Marsters, S., Acosta-Alvear, D., Kimmig, P., Mendez, A.S., Paton, A.W., Paton, J.C., Walter, P., and Ashkenazi, A. (2014). Cell death. Opposing unfolded-protein-response signals converge on death receptor 5 to control apoptosis. Science *345*, 98–101.

Motulsky, H.J., and Brown, R.E. (2006). Detecting outliers when fitting data with nonlinear regression – a new method based on robust nonlinear regression and the false discovery rate. BMC Bioinformatics *7*, 123.

Nakano, K., and Vousden, K.H. (2001). PUMA, a novel proapoptotic gene, is induced by p53. Mol. Cell *7*, 683–694.

Paek, A.L., Liu, J.C., Loewer, A., Forrester, W.C., and Lahav, G. (2016). Cell-to-cell variation in p53 dynamics leads to fractional killing. Cell *165*, 631–642.

Palchaudhuri, R., Lambrecht, M.J., Botham, R.C., Partlow, K.C., van Ham, T.J., Putt, K.S., Nguyen, L.T., Kim, S.-H., Peterson, R.T., Fan, T.M., and Hergenrother, P.J. (2015). A small molecule that induces intrinsic pathway apoptosis with unparalleled speed. Cell Rep. *13*, 2027–2036.

Potapova, O., Basu, S., Mercola, D., and Holbrook, N.J. (2001). Protective role for c-Jun in the cellular response to DNA damage. J. Biol. Chem. *276*, 28546–28553.

Reuven, N., Adler, J., Meltser, V., and Shaul, Y. (2013). The Hippo pathway kinase Lats2 prevents DNA damage-induced apoptosis through inhibition of the tyrosine kinase c-Abl. Cell Death Differ. *20*, 1330–1340.

Roux, J., Hafner, M., Bandara, S., Sims, J.J., Hudson, H., Chai, D., and Sorger, P.K. (2015). Fractional killing arises from cell-to-cell variability in overcoming a caspase activity threshold. Mol. Syst. Biol. *11*, 803.

Sarosiek, K.A., Ni Chonghaile, T., and Letai, A. (2013). Mitochondria: gatekeepers of response to chemotherapy. Trends Cell Biol. *23*, 612–619.

Sharma, S.V., Lee, D.Y., Li, B., Quinlan, M.P., Takahashi, F., Maheswaran, S., McDermott, U., Azizian, N., Zou, L., Fischbach, M.A., et al. (2010). A chromatin-mediated reversible drug-tolerant state in cancer cell subpopulations. Cell *141*, 69–80.

Shaw, S.Y., Blodgett, D.M., Ma, M.S., Westly, E.C., Clemons, P.A., Subramanian, A., and Schreiber, S.L. (2011). Disease allele-dependent small-molecule sensitivities in blood cells from monogenic diabetes. Proc. Natl. Acad. Sci. USA *108*, 492–497.

Sheline, C.T., Behrens, M.M., and Choi, D.W. (2000). Zinc-induced cortical neuronal death: contribution of energy failure attributable to loss of NAD(+) and inhibition of glycolysis. J. Neurosci. *20*, 3139–3146.

Shimizu, S., Kanaseki, T., Mizushima, N., Mizuta, T., Arakawa-Kobayashi, S., Thompson, C.B., and Tsujimoto, Y. (2004). Role of Bcl-2 family proteins in a non-apoptotic programmed cell death dependent on autophagy genes. Nat. Cell Biol. *6*, 1221–1228.

Spencer, S.L., Gaudet, S., Albeck, J.G., Burke, J.M., and Sorger, P.K. (2009). Non-genetic origins of cell-to-cell variability in TRAIL-induced apoptosis. Nature *459*, 428–432.

Sullivan, L.B., Gui, D.Y., Hosios, A.M., Bush, L.N., Freinkman, E., and Vander Heiden, M.G. (2015). Supporting aspartate biosynthesis is an essential function of respiration in proliferating cells. Cell *162*, 552–563.

Suraweera, A., Münch, C., Hanssum, A., and Bertolotti, A. (2012). Failure of amino acid homeostasis causes cell death following proteasome inhibition. Mol. Cell *48*, 242–253.

Taipale, M., Krykbaeva, I., Whitesell, L., Santagata, S., Zhang, J., Liu, Q., Gray, N.S., and Lindquist, S. (2013). Chaperones as thermodynamic sensors of drug-target interactions reveal kinase inhibitor specificities in living cells. Nat. Biotechnol. *31*, 630–637.

Tang, H.L., Tang, H.M., Mak, K.H., Hu, S., Wang, S.S., Wong, K.M., Wong, C.S.T., Wu, H.Y., Law, H.T., Liu, K., et al. (2012). Cell survival, DNA damage, and oncogenic transformation after a transient and reversible apoptotic response. Mol. Biol. Cell *23*, 2240–2252.

Thorburn, J., Andrysik, Z., Staskiewicz, L., Gump, J., Maycotte, P., Oberst, A., Green, D.R., Espinosa, J.M., and Thorburn, A. (2014). Autophagy controls the kinetics and extent of mitochondrial apoptosis by regulating PUMA levels. Cell Rep. *7*, 45–52.

Tyson, D.R., Garbett, S.P., Frick, P.L., and Quaranta, V. (2012). Fractional proliferation: a method to deconvolve cell population dynamics from single-cell data. Nat. Methods *9*, 923–928.

Vanden Berghe, T., Vanlangenakker, N., Parthoens, E., Deckers, W., Devos, M., Festjens, N., Guerin, C.J., Brunk, U.T., Declercq, W., and Vandenabeele, P. (2010). Necroptosis, necrosis and secondary necrosis converge on similar cellular disintegration features. Cell Death Differ. *17*, 922–930.

Wei, M.C., Zong, W.X., Cheng, E.H., Lindsten, T., Panoutsakopoulou, V., Ross, A.J., Roth, K.A., MacGregor, G.R., Thompson, C.B., and Korsmeyer, S.J. (2001). Proapoptotic BAX and BAK: a requisite gateway to mitochondrial dysfunction and death. Science *292*, 727–730.

Wolpaw, A.J., Shimada, K., Skouta, R., Welsch, M.E., Akavia, U.D., Peer, D., Shaik, F., Bulinski, J.C., and Stockwell, B.R. (2011). Modulatory profiling identifies mechanisms of small molecule-induced cell death. Proc. Natl. Acad. Sci. USA *108*, E771–E780.

Yu, Z., Xie, G., Zhou, G., Cheng, Y., Zhang, G., Yao, G., Chen, Y., Li, Y., and Zhao, G. (2015). NVP-BEZ235, a novel dual PI3K-mTOR inhibitor displays anti-glioma activity and reduces chemoresistance to temozolomide in human glioma cells. Cancer Lett. *367*, 58–68.

STAR★METHODS

KEY RESOURCES TABLE

REAGENT or RESOURCE	SOURCE	IDENTIFIER
Bacterial and Virus Strains		
NucLight Red Lentivirus Reagent (EF1a, Puro) Nuclear-localized mKate2 (Nuc::mKate2)	Essen BioSciences	Cat# 4265
Chemicals, Peptides, and Recombinant Proteins		
Sytox Green	Life Technologies	Cat# S7020
Erastin (Compound 13MEW76 in Dixon et al., 2014)	Dixon et al., 2014	N/A
Erastin2 (Compound 35MEW28 in Dixon et al., 2014)	Dixon et al., 2014	N/A
Staurosporine	Sigma-Aldrich	Cat# S6942
Camptothecin	Fisher Scientific	Cat# AC276721000
Etoposide	Sigma-Aldrich	Cat# 12-261-00
Thapsigargin	Sigma-Aldrich	Cat# T9033
Bortezomib	Fisher Scientific	Cat# NC0587961
Zinc Pyrithione	Selleck Chemicals	Cat# S4075
Diethylenetriaminepentaacetic acid	Sigma-Aldrich	Cat# D6518
Ethyl Pyruvate	Sigma-Aldrich	Cat# E47808
1833 Member Bioactive Compound Library (obtained June 2014)	Selleck Chemicals	Cat# L1700
Temozolomide	Selleck Chemicals	Cat# S1237
Fe ICP-MS Standard	ACROS Organics	Cat# AC196051000
Cu ICP-MS Standard	ACROS Organics	Cat# AC195931000
Zn ICP-MS Standard	Fisher Scientific	Cat# PLZN2-2Y
Critical Commercial Assays		
CellTiter-Glo Luminescent Cell Viability Assay	Promega	Cat# G7570
Deposited Data		
Description of the 1,833-member bioactive compound library	Mendeley Data	http://dx.doi.org/10.17632/3pnv5wh5jm.1
U-2 OS^{N} cells + 1,833 bioactive compound library	Mendeley Data	http://dx.doi.org/10.17632/3pnv5wh5jm.1
T98G^{N} cells + DMSO + 1,833 bioactive compound library	Mendeley Data	http://dx.doi.org/10.17632/3pnv5wh5jm.1
T98G^{N} cells + temozolomide (400 μM) + 1,833 bioactive compound library	Mendeley Data	http://dx.doi.org/10.17632/3pnv5wh5jm.1
Experimental Models: Cell Lines		
HT-1080	ATCC	CCL-121; RRID: CVCL_0317
U-2 OS	ATCC	HTB-96; RRID: CVCL_0042
T98G	ATCC	CRL-1690; RRID: CVCL_0556
A549	ATCC	CCL-185; RRID: CVCL_0023
Bax$^{+/+}$ *Bak*$^{+/+}$ SV40 mouse embryonic fibroblasts (MEFs)	ATCC	CRL-2907; RRID: CVCL_U630
Bax$^{-/-}$ *Bak*$^{-/-}$ SV40 MEF	ATCC	CRL-2913; RRID: CVCL_U626
HT-1080^{N}	This Paper	N/A
U-2 OS^{N}	This Paper	N/A
T98G^{N}	This Paper	N/A
A549^{N}	This Paper	N/A
Bax$^{+/+}$ *Bak*$^{+/+}$ MEF^{N} (WT^{N})	This Paper	N/A
Bax$^{-/-}$ *Bak*$^{-/-}$ MEF^{N} (DKO^{N})	This Paper	N/A
Software and Algorithms		
Compound Set Enrichment Analysis. Described in Liu et al., (2013) *Proc Natl Acad Sci*	Broad Institute	genepattern.broadinstitute.org
R	N/A	https://www.r-project.org/
Prism	GraphPad Software	N/A
Excel	Microsoft	N/A

CONTACT FOR REAGENT AND RESOURCE SHARING

Further information and requests for resources and reagents should be directed to and will be fulfilled by the Lead Contact, Scott Dixon (sjdixon@stanford.edu).

EXPERIMENTAL MODEL AND SUBJECT DETAILS

Cell Lines

HT-1080, T98G, A549, U-2 OS, *Bax*$^{+/+}$ *Bak*$^{+/+}$ MEF and *Bax*$^{-/-}$ *Bak*$^{-/-}$ MEF cell lines were obtained from ATCC (Manassas, Virginia, USA). Cell lines were thawed, expanded for one passage and frozen in multiple aliquots that were used in subsequent experiments. All cell lines were grown in humidified tissue culture incubators (Thermo Scientific) at 37°C with 5% CO_2. T98G, A549, *Bax*$^{+/+}$ *Bak*$^{+/+}$ MEF and *Bax*$^{-/-}$ *Bak*$^{-/-}$ MEFs and derivatives were grown in DMEM High-Glucose medium (Cat. No. MT-10-013-CV, Corning Life Sciences, Tewksbury, MA, USA) supplemented with 10% FBS (Cat. No. 26140-079, Life Technologies/Thermo Fisher Scientific, Carlsbad, CA, USA). HT-1080 cells were grown in the same media additionally supplemented with 1% non-essential amino acids (Life Technologies/Thermo Fisher Scientific). U-2 OS cells were grown in McKoy's 5A medium supplemented with 10% FBS. Except where indicated, all media were supplemented with penicillin and streptomycin (Life Technologies/Thermo Fisher Scientific). All cultures were mycoplasma free as confirmed by the absence of bacterial staining when cells were incubated in medium containing the DNA intercalating dye SYTOX Green. Key cancer-associated genes mutated in T98G cells are: *TP53*, *PTEN*, *FAT4*, *NOTCH2*, *AKAP9*, *CLTCL1*, *PER1*, *TCF12*, *FBXO11*, *KMT2C*, *ZFHX3* and *HLA-A*, in U-2 OS cells are: *CTNNB1*, *PREX2*, *PTPN13*, *CCND2*, *LIFR*, *FAT1*, *TSC2*, *SLC34A2*, *ZFHX3*, *TET2* and *PPM1D*, and in A549 cells are: *KRAS*, *KEAP1*, *SUFU*, *ATR*, *STK11*, *POLE*, *SMARCA4*, *CARD11*, *FUS*, *TBL1XR1*, *USP6*, *ERC1*, *CBL*, *FH*, *HIP1*, *PCSK7*, *ZFHX3* and *FLT3* ("cancer census genes", http://cancer.sanger.ac.uk/cosmic, (Forbes et al., 2011)).

METHOD DETAILS

Nuc::mKate2-Expressing Cell Lines

Polyclonal HT-1080, T98G, U-2 OS, A549, *Bax*$^{+/+}$ *Bak*$^{+/+}$ wild-type (WT) MEF and *Bax*$^{-/-}$ *Bak*$^{-/-}$ double knockout (DKO) MEF cell lines expressing nuclear-localized mKate2 (Nuc::mKate2) were generated by lentiviral transduction of a viral vector, at an M.O.I. of 0.3, that directed the expression of nuclear-localized mKate2 (Essen BioSciences, Ann Arbor, Michigan, USA, (Artymovich and Appledorn, 2015)). Polyclonal mKate2-expressing populations were selected using puromycin (1.5 μg/mL, 48-72 h).

Cell Seeding and Compound Addition

Experiments were performed in a high-density, 384-well format. On Day -1 cells grown in T-175 flasks (Fisher Scientific) were trypsinized and counted using a Cellometer Auto T4 cell counter (Nexcelom, Lawrence, MA, USA). 40 μL of cell solution containing the appropriate concentration of cells (e.g. 1,500) was added manually to each well of a glass bottom, 384-well tissue culture plates (Corning, Cat. No. 3712) using a multichannel pipette. The plate was then spun briefly (500 rpm, 2 sec) to settle the cells evenly at the bottom of the wells. Cell death sensitivity can be modulated by high cell number and confluence (Hafner et al., 2016) and we therefore aimed for a starting confluence of less than 50% at the time of drug addition on Day 0 in all experiments. On Day 0, all control and test compounds were prepared in growth medium containing 20 nM SYTOX Green (Life Technologies/Thermo Fisher Scientific). 10-point, 2-fold dilutions were prepared in 384-well storage plates (Thermo Scientific AB-0781) and compounds were added using either a multi-channel pipette or a Versette automated liquid handler configured with a six-position stage and 384-channel head (Thermo Scientific).

Measurement of Cell Viability with PrestoBlue

In control experiments cell viability was measured in HT-1080^{N} cells using resazurin (PrestoBlue, Life Technologies/Thermo Fisher Scientific). The day before compound addition, 40 μL of cells were seeded into a 384-well plate at a concentration of 1,500 cells/well and then treated with compounds. Following compound incubation, 10 μL of a 50/50 v/v medium/PrestoBlue solution was added to each well using a Versette automated liquid handler (Thermo Scientific) and incubated for 2 hours in a tissue culture incubator maintained at 37°C with 5% CO_2. Fluorescence readings were made using a Cytation3 multimode plate reader (BioTek, Winooski, VT, USA) set to ex/em of 530/590 nm.

STACK Data Acquisition and Analysis

Acquisition of Population Images

In our current implementation, live and dead cell counts were obtained over time using an IncuCyte Zoom dual color live content imaging system (Model 4459, Essen BioSciences, Ann Arbor, USA) residing within a Thermo tissue culture incubator maintained at 37°C with 5% CO_2. Data were acquired using a 10x objective lens in phase contrast, green fluorescence (ex: 460 ± 20, em: 524 ± 20, acquisition time: 400 ms) and red fluorescence (ex: 585 ± 20, em: 665 ± 40, acquisition time: 800 ms) channels. Images (1392 x 1040 pixels at 1.22 μm/pixel) were acquired from each well at set time intervals. Data acquisition time per well was less than two seconds.

Live and Dead Cell Counting and Confluence Measurements

Automated image analysis routines were empirically optimized for each cell line using the Zoom software package (V2016A/B) and training data from DMSO and lethal compound-treated samples. The mechanism of mKate2$^+$ protein loss from the nucleus during cell death could involve disruption of nuclear import, increased nuclear membrane permeability or proteolytic destruction of the protein (Faleiro and Lazebnik, 2000; Kihlmark et al., 2004) and may vary between cell lines and lethal perturbations. The detection of live and dead cells was therefore optimized for each cell line. WT^N MEF and DKO^N MEF populations were analyzed using a routine with the following settings (in parentheses) to count mKate2$^+$ objects (Parameter adaption, threshold adjustment: 1; Edge split on; Edge sensitivity 50; Filter area min 50 μm^2, maximum 2000 μm^2; Eccentricity max 1.0) and SG$^+$ objects (Parameter adaption, threshold adjustment: 10; Edge split on; Filter area min 30 μm^2, maximum 750 μm^2; Eccentricity max 0.9). In some experiments, double-positive mKate2$^+$/SG$^+$ objects (overlaps) were identified by the overlap of red and green objects defined above (overlap area min 50 μm^2). HT-1080^N, U-2 OS^N and A549^N populations were analyzed using a routine with the following settings (in parentheses) to count mKate2$^+$ objects (Parameter adaption, threshold adjustment: 1; Edge split on; Edge sensitivity 50; Filter area min 20 μm^2, maximum 800 μm^2; Eccentricity max 1.0) and SG$^+$ objects (Parameter adaption, threshold adjustment: 10; Edge split on; Filter area min 5 μm^2, maximum 800 μm^2; Eccentricity max 0.9). The nuclei of T98G^N cells were more complex, and the following settings were used in these cells to identify mKate2$^+$ objects (Threshold adjustment: 2.5; Edge split on; Edge sensitivity -31; Hole fill 0; Filter area min 100 μm^2, maximum 800 μm^2; Eccentricity max 0.9) and SG$^+$ objects (Threshold adjustment: 10; Edge split on; Edge sensitivity -5; Hole fill 0; Filter area min 20 μm^2, maximum 750 μm^2; Eccentricity max 0.9). In some experiments we measured confluency of the cultures (segmentation adjustment, background: 1.8; Cleanup, hole-fill: 400 μm^2; Filter, minimum area: 200 μm^2). mKate2$^+$ and SG$^+$ counts, expressed as objects per mm^2, and confluence measures, expressed as an overall percentage (0%–100%), were exported to Excel (Microsoft) for further processing. Counts more than 10-fold different than the one immediately preceding in the time course were censored. This affected less than 0.001% of all counts and were due to transient technical issues with data acquisition (e.g. an image out of focus for one scan). Widespread cell detachment prior to death, which would be detected by a decrease in mKate2$^+$ counts with no corresponding increase in SG$^+$ counts, was not observed in these experiments.

Lethal Fraction Scoring

At any given time point n in a treatment time course (t = 0 → t = n), the lethal fraction (LF) is given by Equation 1.

$$LF_{t=n} = 1 - \frac{mKate2^+_{t=n}}{\left(SG^+_{max_{t=0 \rightarrow t=n}} + mKate2^+_{t=n}\right)} \quad \text{(Equation 1)}$$

Some treatments result in the loss of SG$^+$ signals from long dead cell corpses. Thus, when computing the lethal fraction at a given time the maximum number of SG$^+$ objects from the start of that experiment is used. This equation does not consider SG$^+$/mKate2$^+$ double-positive cells separately. Large numbers of persistent SG$^+$/mKate2$^+$ double-positive cells would lead to an underestimation of cell death. This potential confound must be accounted for when optimizing image segmentation and counting routines for each cell line. The maximum lethal fraction, hereafter LF_{max}, equals to the highest individual LF score at any point in a time course and is extracted directly from a set of LF scores over time by applying the MAX function in Microsoft Excel 14.6.0 (Microsoft). Area under the curve values were computed from LF curves over time using the trapezoidal method implemented in Prism 6.0h (GraphPad Software, Inc).

Parameterization Using the Lag Exponential Death (LED) Model

LF scores over time were parameterization using the LED model given by Equation 2:

$$LF(t) = LF_0 + (LF_P - LF_0)\left(1 - e^{-D_R(t-D_O)}\right) \quad \text{(Equation 2)}$$

Where t is time, D_O is the time at which the exponential increase in LF begins, LF_0 is the average LF value up to D_O, LF_P is the plateau LF value, and D_R is the maximum cell death rate. These calculations were performed using the plateau followed by one-phase association function in Prism 6.0h (GraphPad Software), with D_O unconstrained and LF_P constrained to be ≤ 1. LF_0 was also left unconstrained and can be non-zero due to background (basal) levels of cell death within a population, or in response to compounds that initiate substantial cell death by the first measurement (e.g. ROLs). Three notes: (i) LF_P approximate but do not equal LF_{max} values derived directly from LF scores over time. LP_P values are obtained from curves successfully fit with the LED model, and they cannot be obtained in cases where the LED model produces ambiguous fits. Thus, in this work we typically report the exact LF_{max} values; (ii) different absolute levels of cell death (i.e. LF_P) can be associated with the same D_O or D_R values. Fits flagged as ambiguous is Prism were not used in these analyses. Fits to other models (e.g. sigmoidal) were likewise examined using Prism 6.0h.

Bioactive Compound Profiling and Analysis

Compound Library

A bioactive compound library (Cat. No. L1700) was obtained from Selleck Chemicals (Houston, TX) and stored at -80°C. The details of this library can be found in the Data Repository associated with the work. The library was re-formatted from 96-well to 384-well format using a Versette automated liquid handler configured with a 96 channel pipetting head, and diluted to 2 mM in DMSO.

Data Collection

Data were collected as described above, with the following additional information. The day before compound addition, T98G^N or U-2 OS^N cells were seeded into five 384-well plates at a concentration of 1,500 cells/well at a final volume of 40 µL. The next day

compounds were added from freshly thawed library master stock plates using a Versette liquid handler equipped with a 384-channel pipetting head. The final concentration of each library compound in each well was 5 μM. In one experiment with $T98G^N$ cells, library compounds were added to medium containing 400 μM of temozolomide. Plates were then imaged immediately and every 4 h ($T98G^N$) or 2 h (U-2 OS^N) thereafter for a total of 96 h ($T98G^N$) or 118 h (U-2 OS^N). The experiment was carried out for longer in U-2 OS^N cells as they were observed to proliferate more slowly than $T98G^N$.

Data Processing

All STACK data were exported as counts of SG^+ and $mKate2^+$ objects/mm^2 and data files from each plate were re-organized using R (r-project.org) and then analyzed further using Excel and Prism 6.0h. Eight library compounds that generated significant green background fluorescence in $T98G^N$ cells were identified by visual inspection of wells with high apparent starting SG^+ counts (>50 Obj/mm^2 at t = 0 or 4 h) in the absence of evident cell death, as judged by $mKate2^+$ counts at t = 0 or 4 h, and removed from further analysis (PHA-665752, idarubicin HCl, TSU-68, quinacrine 2HCl, Ro 31-8220 mesylate, daunorubicin HCl, sunitinib malate, SU11274 and nintedanib). In the U-2 OS^N experiment, seven compounds were removed from the analysis for this reason (nintedanib, PHA-665752, TSU-68, idarubicin HCl, SB216763, SU11274 and Ro 31-8220 mesylate). From both experiments we also eliminated a small number of wells where variation in cell seeding resulted in < 50 or > 400 $mKate2^+$ Obj/mm^2 at t = 0. We confirmed by ROUT analysis ((Motulsky and Brown, 2006), Q = 1%) that this resulted in datasets free from cell number outliers.

Identification of High Confidence Lethal Compounds in U-2 OS^N and $T98G^N$ Cells

For each screen the set of DMSO control populations (n = 79 for U-2 OS^N, n = 87 for $T98G^N$) distributed throughout all five assay plates were used as negative controls and, more specifically, as a means to assess background cell death (e.g. due to nutrient depletion and overcrowding). These DMSO controls were normally distributed (D'Agostino & Pearson omnibus normality test, $P > 0.05$) and therefore compounds with LF_{max} scores > 3 standard deviations (SD) from the mean of the DMSO controls were considered high confidence lethal compounds. For the $T98G^N$ + DMSO experiment this corresponded to LF_{max} thresholds of 0.578, 0.514, 0.402, 0.554 and 0.595 for plates one to five, respectively; in U-2 OS^N cells the corresponding thresholds were 0.073, 0.104, 0.103, 0.079 and 0.087 for plates one to five, respectively. The low values in the U-2 OS^N experiment reflected the limited cell death experienced by U-2 OS^N populations over the course of the experiment. Our goal was to examine only those compounds that produced substantial lethality within the timeframes of the experiments. Therefore, to arrive at a final list of candidate lethal compounds we applied a minimum $LF_{max} > 0.5$ cut-off to select only those compounds exhibiting at least 50% cell death. This eliminated four compounds from plate three in the $T98G^N$ experiment, and a large number of compounds from the U-2 OS^N experiment with LF_{max} values greater than the plate-specific 3xSD LF_{max} thresholds, but below 0.5. These weaker lethal compounds were not studied further here.

Comparative Analysis of Cell Death Kinetics in U-2 OS^N and $T98G^N$ Cells

140 high-confidence lethal compounds were identified in both U-2 OS^N and $T98G^N$ experiments. 80 were common to both experiments, referred to as common high-confidence lethal compounds. LED models produced unambiguous fits to LF scores over time for 139/140 compounds in U-2 OS^N and 136/140 compounds in in $T98G^N$. Three compounds (elaiophylin, BGT226 and dioscin) triggered cell death with an essentially instantaneous onset in $T98G^N$ cells, resulting in ambiguous fits. Because these compounds were clearly highly lethal, they were arbitrarily assigned D_O values = 1 h and included in the set of high confidence lethal compounds for this cell line. Despite the ambiguous curve fits, manual inspection indicated that the computed D_R values were representative of the initial maximal rate of cell death for these three compounds and used in subsequent comparative analyses.

Estimation of Expected Drug Combination Effects

From LF curves we computed AUC and LF_{max} values for populations treated with DMSO alone (D), library compound alone (L) or TMZ alone (T). LF_{max} and AUC values are obtained directly from LF scores and do not require curve fitting, which is inappropriate for conditions that induce minimal lethality. Using either AUC or LF_{max} values as inputs, we computed the expected compound interaction (CI_e) between TMZ and each library compound using the formula: $CI_e = L + (T\text{-}D)$. ΔAUC and ΔLF_{max} values were computed as the difference between the expected interaction, CI_e, computed as described above, and the observed AUC or LF_{max} for the combination of TMZ and each library compound. Enhancing interactions had positive ΔAUC and ΔLF_{max} values and suppressive interactions had negative ΔAUC and ΔLF_{max} values. Significant compound interactions were identified using two methods. In one method, ΔAUC and ΔLF_{max} scores for the 87 control conditions were used to establish 99% confidence thresholds (mean + 3 standard deviations) resulting in thresholds of $|\Delta AUC| > 8.8$, $|\Delta LF_{max}| > 0.23$. When applied to our dataset, these thresholds excluded all control treatments, as expected. The second method, ΔAUC values for each compound were used as input for CSEA analysis, as described below.

Compound Set Enrichment Analysis (CSEA)

CSEA was performed as described (Liu et al., 2013; Shaw et al., 2011). From the library of 1,833 bioactive compounds, 428 have no known mammalian target. Of the remaining 1,405 compounds, we could assign 1,082 into one of 70 different target classes with ≥ 5 members (median = 10.5) on the basis of known or putative molecular targets. Target assignments were made on the basis of manual annotation of each compound, together with information provided by the library supplier (SelleckChem). For the purposes of CSEA, compounds were assigned to single groups on the basis of the best target (i.e. target against which the compound showed the greatest potency) using data made available on the SelleckChem website. Certain inhibitors were grouped into larger superfamilies (receptor tyrosine kinase (RTK) inhibitors or non-receptor tyrosine kinase inhibitors (NRTK)). These and other compounds likely inhibit more than one target in cells. For CSEA analysis we did not remove compounds whose behavior were outliers relative to other members of the same group (e.g. epoxomicin relative to other proteasome inhibitors). CSEA analysis was performed using the GSEAPreranked module (genepattern.broadinstitute.org). LF_{max} values were used in separate analyses as ranking variables. Default

settings were employed with the exception of the 'min gene set size', which was set equal to 5, which experience suggested was the minimum required to obtain sufficient statistical power to accurately distinguish between classes.

Identification of Rapid Onset Lethal (ROL) and Slow Onset Lethal (SOL) Compounds

ROL and SOL compounds were identified using data collected from the profiling of the 1,833-member bioactive compound library in $T98G^N$ and U-2 OS^N populations, described above. LF curves for all high-confidence lethal compounds identified in both experiments were parameterized using LED models and D_O parameter values extracted. As noted, certain compounds were near-instantaneously lethal in $T98G^N$ cells (BGT226, elaiophylin, dioscin), as determined by visual inspection. D_O values could not be computed and in these cases D_O were arbitrarily set to 1 h. Compounds were ranked according to D_O values and those in the bottom 25% percentile were considered ROL compounds, while those above the 75% percentile were considered SOL compounds.

Analysis of ROL Cell Death Modulatability

Modulatability of cell death was assessed using WT^N and DKO^N MEFs. Cells were treated with lethal compounds and monitored every 2 h for 48 h using STACK. Lethal compounds were tested in 10-point, 2-fold dose-response series: elaiophylin (high concentration: 20 μM), BGT226 (high concentration: 20 μM), pacritinib (high concentration: 20 μM), zinc pyrithione (ZP, high concentration: 20 μM). Btz (high concentration: 1 μM) and erastin (high concentration: 20 μM) served as controls for apoptotic and non-apoptotic cell death. Cell death with and without the pan-caspase inhibitor Q-VD-OPh was also analyzed every 2 h for 48 h using STACK and the following concentration of each ROL or control compound: elaiophylin (312 nM), BGT226 (312 nM), pacritinib (5 μM), zinc pyrithione (1.25 μM), bortezomib (200 nM) or erastin (63 nM). LF scores and AUC values were computed for each compound concentration as described above.

Seahorse Assay

Metabolic profiles over time were analyzed using Seahorse technology. $A549^N$ or $T98G^N$ cells were seeded at 10,000 cells/well into Seahorse XFp cell culture miniplates in a final volume of 80 μL, briefly spun at 500 RPM, and allowed to settle overnight at 37°C and 5% CO_2. 200 μL of XF calibrant (pH 7.4) was added to an XFp extracellular flux cartridge and left at 37°C in the absence of CO_2. The next day, cells were washed twice with 200 μL of Seahorse medium (XF Base Medium Minimal DMEM, 25 mM glucose, 1.0 mM sodium pyruvate, 4 mM glutamine, pH 7.4). After washing, each well was incubated in 180 μL Seahorse medium. At this point, the wells were imaged using the IncuCyte to obtain $mKate2^+$ live cell counts that were used for normalization. The cell culture miniplate was allowed to incubate at 37°C in the absence of CO_2 for one hour prior to the beginning of the experiment. Test compounds were prepared at 10x in Seahorse medium in a final volume of 20 μL in the XFp extracellular flux cartridge to be injected later in the experiment. Oxygen consumption rate (OCR) and extracellular acidification rate (ECAR) was monitored every six minutes for 60 minutes pre-compound injection and for 420 minutes post-compound injection (FCCP/Oligomycin stressor mix final concentration = 2/1 μM and ZP final concentration = 10 μM). ZP-induced cell death was not appreciable over the course of this experiment and OCR and ECAR were therefore normalized to cell number at t = 0, measured by counting live cell numbers by imaging (see above).

Measurements of Intracellular Metal Levels

Measurements were performed at the Stanford Environmental Measurements Facility. Measurements were carried out using inductively coupled plasma mass spectrometry (ICP-MS) with an XSERIES 2 ICP-MS (Thermo Scientific, USA). Samples were run along with four serially diluted standards of Fe, Cu, and Zn in 2% nitric acid and 2% nitric acid blank. Standards were obtained as 1 mg/mL stocks in 2% nitric acid from ACROS Organics (Fe and Cu, AC196051000 and AC195931000) or CertiPrep (Zn, PLZN2-2Y). Samples were collected from $A549^N$ and $T98G^N$ cells seeded at 250,000 cell/well in 6-well dishes at a final volume of 2 mL. The next day, cells were washed once with warm HBSS, followed by addition of fresh media (or fresh media supplemented with ethyl pyruvate) ± drug or vehicle. For conditions with ethyl pyruvate, the same DMEM medium used to culture cells was used to produce a stock of 20 mM ethyl-pyruvate supplemented media. Cells were treated for 2 h followed by wash with ice cold HBSS and lysed in 500 μL of redistilled 70% nitric acid (≥ 99.999%, Sigma) for 16-20 h. Samples were subsequently diluted to 2% nitric acid using HPLC Grade submicron filtered water (Fisher Scientific).

Measurement of ATP Levels

The day before compound addition, 40 μL of cells were seeded into a 384-well plate at a concentration of 1,500 cells/well. The next day, cells were treated with vehicle control or test compounds for a given length of time followed by a 30 min incubation at room temperature to equilibrate the plate to room temperature. After the equilibration to room temperature, 40 μL of CellTiter-Glo reagent (Promega) was added to each well and mixed for 2 min. The mixture was allowed to equilibrate for an additional 10 minutes prior to taking a luminescence measurement. Luminescence was measured using a Cytation3 multimode plate reader (BioTek, Winooski, VT, USA) set to luminescence, optics position = top, gain = 135. ATP values are expressed as a percentage of the DMSO control.

QUANTIFICATION AND STATISTICAL ANALYSIS

Lethal fraction scoring was performed using Excel 14.6.0. LED curve fitting was performed using Prism 6.0h. Images were processed using Adobe Photoshop (Adobe Systems, San Jose, CA). Figures were assembled using Adobe Illustrator. Graphing and all statistical

analyses were performed using Prism 6.0h. Except where noted, all data represent mean ± S.D of three biological replicates. Additional statistical details are found in the Results, STAR Methods, and Figure legends.

DATA AVAILABILITY

For the 1,833-member bioactive compound screens in U-2 OS^N and $T98G^N$ cells (both DMSO only and temozolomide (TMZ)-treated) all live and dead cell counts, as well as calculated lethal fraction scores and AUC values, are available online via the Mendeley Data repository (http://dx.doi.org/10.17632/3pnv5wh5jm.1).